International Journal of Engineering Trends and Technology
ISSN: 2231–5381 / https://doi.org/10.14445/22315381/IJETT-V71I10P206

Volume 71 Issue 10, 60-70, October 2023

Original Article

Computer-Aided Diagnosis Model for Lung Diseases Using Sea Lion Optimization with Deep Convolutional Recurrent Neural Network on Chest X-ray Images

S. Vidyasri[1], S. Saravanan[2]

[1,2]*Department of Computer and Information Science, Faculty of Science, Annamalai University, Annamalai Nagar, Tamilnadu, India.*

[1]*Corresponding Author : thirukamusaipriya1991@gmail.com*

Received: 26 June 2023 Revised: 30 August 2023 Accepted: 15 September 2023 Published: 03 October 2023

Abstract *- Lung Disease (LD) is the leading factor of increasing death rates across the world and incorporates tuberculosis diseases, pneumonia, COVID-19, and pneumothorax. Prompt and early diagnosis of LD can probably reduce the risk of death and improve the patient's quality of life. Current medical image modalities and imaging tests seem to be effective tools that can help medical practitioners detect different conditions. Computed Tomography (CT) and Chest X-ray (CXR) radiographic images usually use image modalities. These diagnostic tools allow clinicians to look at the internal structure of the body without the need for cutting. Recently, Convolutional Neural Networks (CNNs) have become the potential technique of Computer Vision (CV) and have reached promising outcomes in medical image diagnosis. This study designs an Automated Lung Disease Detection Using Sea Lion Optimization with Deep Convolutional Recurrent Neural Network (SLO-DCRNN) technique on CXR images. In the presented SLO-DCRNN model, the DL and hyperparameter tuning process can be employed for automated LD. At the initial stage, the SLO-DCRNN model uses the Adaptive Weiner Filter (AWF) technique to eliminate the noise level that exists in the images. Next, the SLO-DCRNN method exploits the Neural Architectural Search Network (NASNet) Large model for feature vector generation. Followed by the DCRNN approach is utilized to identify different kinds of LDs. At last, the SLO system was enforced for the tuning process of the DCRNN approach. An extensive set of investigations was performed to demonstrate the superior result of the SLO-DCRNN technique. The simulation results ensured the improvement of the SLO-DCRNN technique over other existing systems.*

Keywords *- Lung diseases, Deep learning, Medical imaging, Sealion optimizer, Chest X-ray images.*

1. Introduction

Detection of LD is presently accomplished over an investigation of CXR imageries performed by a qualified radiologist because of its comfort and non-surgical valuation for comprehensive discoveries of the chest condition in short [1]. Also, it is appropriate for subsequent investigation since variations of the ailment can be detected further initially and effortlessly. The typical imaging procedure for diagnosing LD comprises CT, Magnetic Resonance Imaging (MRI), and CXR scan [2]. Though CT and MRI scans are presently the best regulations in evaluating LDs, these also come with very high prices that encompass radiation exposure and are not promptly accessible worldwide [3]. Comparatively, CXRs are less priced, promptly obtainable, and one of the majorly available diagnostic imaging methods for pulmonary and cardiothoracic disorders. Hence, clinical imaging procedures, e.g., CXR, play a crucial part in diagnosing persons as there is a high suspicion of contamination under risk factors and symptoms [4], excluding children and expectant women outside of emergency conditions. CXR images have been discovered in the current epidemic to detect LDs.

Classification and detection of LDs by employing CXR imageries is a convolutional method for radiologists [5]. Hence, this earned noteworthy consideration from the scientists to develop automatic detection of LD procedures. Subsequently, several CAD structures have been presented for detecting LD in the past decade by implementing X-ray images [6]. However, such methods were unsuccessful in attaining the needed performance for detecting LD and its classification. The recent COVID-19-associated lung infections have made these tasks very demanding for such CAD procedures. It becomes very critical in detecting the presence of pneumonia in the lungs and its further classification into COVID-19, viral, and bacterial diseases. This structural classification also delivers suitable medical care to patients with pneumonia [7]. Many works have been conferred with CAD structures for COVID-19, and DL

procedures and automated image processing have been established for detecting the disease of pneumonia by adopting CXR images. Several automatic tools also exist for the efficient detection of LD and classification. Despite DL and ML modalities prevailing in previous studies [8], improving the accomplishment of the classification of LD is still required. Due to the constant development of the procedure, the amount of restrictions of DL procedures also surges promptly, resulting in procedural overfitting. Concurrently, diverse hyperparameters have a key result in the CNN's proficiency procedure [9]. Especially parameters like batch size and epoch count are also critical in obtaining an effective result. As the R and D process for hyperparameter tuning is an exhausting and inaccurate procedure, metaheuristic approaches can be enforced [10]. Hence, in this process, a metaheuristic approach is implemented to select parameters of the DL procedures.

This study designs an Automated Lung Disease Detection Using Sea Lion Optimization with Deep Convolutional Recurrent Neural Network (SLO-DCRNN) technique on CXR images. In the presented SLO-DCRNN technique, the SLO-DCRNN technique uses the Adaptive Weiner Filter (AWF) technique to eliminate the noise level that exists in the images. Next, the SLO-DCRNN technique exploits the Neural Architectural Search Network (NASNet) Large model for feature vector generation. Followed by the DCRNN approach is utilized to identify different kinds of LDs. Finally, the SLO system was enforced for the tuning process of the DCRNN approach. An extensive set of investigations was performed to demonstrate the superior result of the SLO-DCRNN technique.

2. Related Works

Vaiyapuri et al. [11] presented a CSO-CADLCC algorithm called cat swarm optimization-related CAD technique for classifying LDs. The presented approach uses the Gabor filtering-based noise elimination approach for preprocessing the dataset. Likewise, using the NASNetLarge method, preprocessed imageries feature extracting process can be done. [12] The technique is followed by the CSO technique, having a Weighted ELM (WELM) module, which is used for classifying lung nodules. Eventually, for the tuning parameter of the WELM model, the CSO technique was leveraged, resulting in an improved classification outcome. In [13], modelled a deep CNN to lung cancer related to global factors of CT images based on the original DCNN and for validating the feasibility of DCNN, effects of optimization algorithm, diverse model parameters, and model structure on the detection accomplishment were deliberated and applied used and render a reference on CAD of lung cancers.

Yang et al. [14] introduced a set of segmentations or annotations of lung radiological manifestation that are reliable with TB in the openly accessible and broadly utilized Shenzhen CXR database. [15] The aim of releasing such annotations was to develop the existing image segmenting techniques to enhance the outcome of fine-grained segmentation of TB-consistent findings in digitalized CXR imageries. In [16], the authors have modelled new metrics that implement various weights on deviations of features. For deriving Weighted City Block Distance (WCBD) and Weighted Euclidean Distance (WED), the weights were utilized correspondingly with city block distance and Euclidean distance.

In [17], a CAD scheme was devised to enhance the consistency and diagnostic accuracy in image interpretation of pulmonary tuberculosis. Utilizing edge reconstruction region and growing algorithms, the lung fields were segmented. From the diseased regions, texture features were derived and manifested as nodular opacities, consolidations, and cavitation. A wrapper technique that combined a one-against-all Support Vector Machine (SVM) classifier and Cuckoo Search Optimization Algorithm (CSA) was utilized for choosing the optimal feature subset. First, using entropy, CSA is applied, and second, without utilizing entropy measure. Utilizing a one-against-all SVM classifier, training is done with selective attributes. Mique and Malicdem [18] concentrated on formulating a method that segments the pulmonary from CXR imageries. Utilizing residual U-Net structure-based semantic segmentation, the authors can train and develop a method utilizing a set of lung masks and 562 CXR images.

3. The Proposed Model

In the present article, a novel SLO-DCRNN approach was presented to identify and classify LDs on CXR images accurately. The proposed SLO-DCRNN approach can employ the DL and hyperparameter tuning process for automated LDs. It follows a series of operations such as AWF-based noise removal, NASNet large feature extraction, SLO-based tuning process, and DRCNN classification. Figure 1 represents the workflow of the SLO-DCRNN algorithm.

3.1. Image Preprocessing

Initially, the AWF technique is applied to remove noise that exists in it. The first method designed to denoise in digital images depends on Wiener filtering. Considering (n_1, n_2) as a specific pixel location, the AWF is represented as follows [19]:

$$AWF\ [I(n_1, n_2)] = \mu + \frac{\sigma^2 - \sigma_n^2}{\sigma^2}(I(n_1, n_2) - \mu) \qquad (1)$$

In Equation (1), I, (σ^2), and μ signifies the image of the input discrepancy, and the mean is estimated locally from the $(N \times M)$ local neighbourhood set of all the pixels.

$$\mu = \frac{1}{MN} \sum_{n_1, n_2 \varepsilon \aleph} I\,(n_1, n_2) \qquad (2)$$

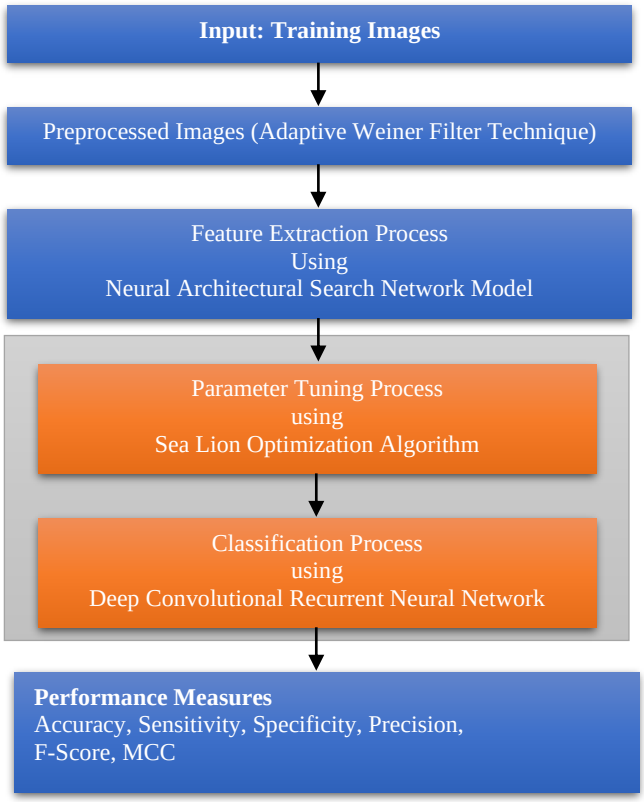

Fig. 1 Workflow of SLO-DCRNN approach

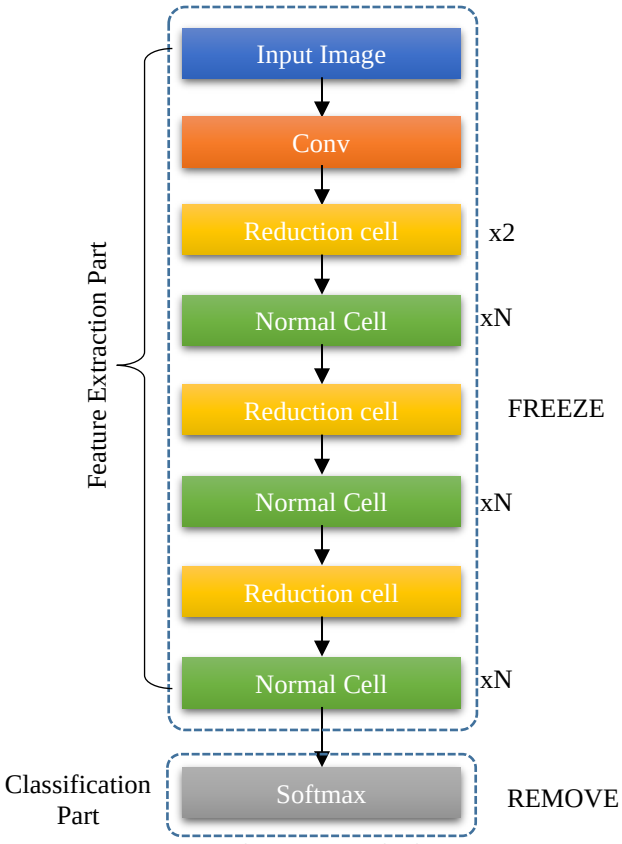

Fig. 2 Architecture of NASNet used for feature extraction

$$\sigma^2 = \frac{1}{MN} \sum_{n_1,n_2 \varepsilon \aleph} I^2 (n_1, n_2) - \mu^2 \quad (3)$$

Where (σ_n) denotes the variance of the noise.

3.2. Feature Extraction using NASNet Large

The SLO-DCRNN technique employed the NASNet Large model for feature vector generation in this phase. In general, a NASNet is a CNN approach based on reinforcement learning and a scalable NAS approach [20]. The study proposed a NASNet Large CNN model using NAS methodology. It was introduced by Google's AI research team in 2017. The architecture of NASNet Large consists of a sequence of repeating blocks, each containing multiple parallel convolutional layers. The key idea behind NASNet is to automatically discover the optimal architecture through a search process rather than relying on human-designed architectures. The initial stage of the NASNet architecture is a stem convolutional block that processes the input image. It applies several convolutional layers with different filter sizes to capture features at various scales. The repeating blocks in NASNet Large are called "cells." These cells are constructed using a combination of normal and reduction cells. The normal cells are responsible for capturing fine-grained features, while the reduction cells are designed to reduce spatial dimensions and capture more global features. Each cell consists of multiple nodes, and each node operates on the outputs of its preceding nodes. These operations can include various types of convolutions, pooling, and skip connections. During the search process, the operations for each node are determined based on their performance in a validation set. NASNet Large utilizes a technique called "sequential model-based optimization" to iteratively search for the best-performing cell architectures. This optimization process involves training and evaluating multiple candidate architectures to find the one with the highest accuracy. NASNet Large plays a crucial role in feature extraction for image classification tasks. As a CNN architecture, NASNet Large is specifically designed to extract meaningful and discriminative features from input images.

In NASNet Large, the repeating blocks or cells are responsible for feature extraction. Each cell contains multiple nodes, and each node operates on the outputs of its preceding nodes. These operations include convolutions, pooling, and skip connections. During the search process of NASNet, the architecture is optimized to identify the most effective operations at each node. This optimization is based on the performance of the candidate architectures on a validation set. As a result, NASNet Large automatically discovers and incorporates the most relevant and informative operations for extracting features from images. Using a combination of normal and reduction cells, NASNet Large captures features at different scales. The normal cells focus on fine-grained details, while the reduction cells reduce spatial dimensions and capture more global features. This multi-scale approach enables the network to learn both local and global features,

leading to a more comprehensive representation of the input images. The learned features from NASNet Large can then be passed to a classifier layer, typically consisting of fully connected layers, to make predictions for image classification tasks. The classifier layer takes the high-level features learned by the network and maps them to specific classes or labels.

In NASNet Large, the earlier networking layers are typically frozen during feature extraction, while the later layers are fine-tuned. This approach is known as transfer learning, where pre-trained layers from a large dataset are utilized as an initial point for a novel task. Freezing layers means their weights and biases are not updated during training. By freezing the earlier layers, the network retains the pre-learned low-level features. It avoids overfitting the new dataset, allowing it to focus on learning task-specific features in the subsequent layers, as shown in Figure 2.

In NASNet Large, the initial layers, such as the stem convolutional block and the early cells, which capture basic image features like edges, textures, and colours, are typically frozen. These layers are considered to be more generic and transferable across different tasks. On the other hand, the later layers, including the deeper cells and the classifier layers, are fine-tuned. Fine-tuning involves updating the weights and biases of these layers using the novel dataset to adapt the network to the specific classification task. By freezing the earlier layers and fine-tuning the later layers, NASNet Large takes advantage of the pre-learned features while allowing the network to specialize in learning task-specific features. This approach helps achieve better performance with less training data and computational resources.

3.3. Hyperparameter Tuning using SLO Algorithm

In this work, the SLO technique was applied for the tuning process of the DCRNN technique. SLO stimulates the hunting behaviour of sea lions by the method by which it is captured and encircles prey or exploits their whiskers and tails [21]. While working on different benchmark functions, SLO could offer more competitive results than other PSO algorithms. SLO includes the vocalization phase, detecting and tracking phase, searching for prey, and attacking phase are given below.

3.3.1. Detecting and Tracking Phase

Initially, SLO creates N (the population size) and D-dimensional solutions based on the uniform distribution in the search space. Next, recognize the prey's position and collect other individuals joining the group to organize. The prey assumed the current optimum solution or the solution nearby to the optimum result. This behaviour is shown in Equation (5).

$$X_{i,j}^{init} = X_{i,j}^{\min} + rand_{i,j}\left(X_{i,j}^{\max} - X_{i,j}^{\min}\right) \quad (4)$$

In Equation (4), $X_{i,j}^{\min}$ and $X_{i,j}^{\max}$ represents the minimal and maximal value for the j[th] parameter of the i[th] solution; $rand$ denotes the unchanging randomized value within $[0,1], i = 1,2,\dots,N,\ j = 1,2,\dots,D$, $X_{i,j}^{init}$ denotes the initial location vector of $i\text{-}th$ solution.

The solution is estimated for fitness using the objective function.

$$X^{g+1} = X_{best} - C|2rX_{best} - X^{g}| \quad (5)$$

$$C = 2\left(1 - \frac{g}{g_{\max}}\right) \quad (6)$$

Where X_{best}^{g} denotes the location vector of the optimum solution; X^{g} indicates the individual in iteration g; g represents the existing iteration of the generation; $g_{\max}$ shows the maximal amount of generations; r indicates a random number within$[0,1]$; X^{g+1} represents the newest location of the searching agent afterwards upgrading; C denotes a parameter linearly reduced from two to zero, specifying the sea lion's encircling method once they draw near and encircle the prey.

3.3.2. Vocalization Stage

Once an individual identifies a group of prey, it calls other individuals to collect and generate a net for the prey's capture, and that sea lion is regarded as a leading entity and leads the group and decides the behaviours of the group as follows.

$$SP_{leader} = |(V_1(1 + V_2)/V_2| \quad (7)$$

$$V_1 = \sin(\theta) \quad (8)$$

$$V_2 = \sin(\phi) \quad (9)$$

Where θ indicates the voice refection's angle from the water; (ϕ) denotes the voice refraction's angle from the water and SP_{leader} denotes the decision of the leader than other individuals in the group.

3.3.3. Attacking Phase (Exploitation Phase)

The sea lion's hunting activity led by the leader is discussed in the following:

Dwindling encircling strategy: These behaviours rely on the value of C and are linearly reduced within [0,2]; hence, this enables the search space nearby the present optimum location to force and shrink other search agents for updating.

Thus, a new upgraded location of the sea lion is positioned anyplace in the searching range amongst its existing location and the position of the optimum agent.

Circling updation location: Sea lion chases the prey's bait ball and hunts them beginning from the end using Equation (10), with m a randomly generated integer within $[-1, 1]$.

$$X^{g+1} = X_{best} + \cos(2\pi m)|X_{best} - X^{g}| \quad (10)$$

3.3.4. Searching for Prey (Exploration Step)

During the discovery stage, the search agent upgrades the position by randomly selecting the sea lion:

$$X^{g+1} = X^{g}_{rand} - C\left|2rX^{g}_{rand} - X^{g}\right| \quad (11)$$

The condition which enables the exploitation stage to occur is once the value of C develops larger than 1. Equation (11) X^{t}_{rand} denotes a randomly chosen individual from the existing population. r denotes the random value within[0,1]. The SLO manner produces a Fitness Function (FF) for accomplishing enhanced classifier results. It explains the positive integer for representing the better efficiency of the solution candidate. In such cases, minimizing the classifier rate of errors is regarded as FF provided in Equation (12).

$$fitness(x_i) = ClassifierErrorRate(x_i) = \frac{no.of\ misclassified\ instances}{Total\ no.of\ instances} * 100 \quad (12)$$

3.4. Image Classification

In this work, the DCRNN is exploited for the identification of different kinds of LDs and comprises four major parts [22]:

(1) an SFLN with sigmoid activation reads the last output of recurrent layers and calculates the possibility of the Event Activity (EA) for all the frames;

(2) a time-frequency of the dataset is given to $L_c \in \mathbb{N}$ convolution layers with non-overlapping pooling on Frequency Axis (FA);

(3) EA probability is binarized by thresholding on constant to accomplish EA prediction, and

(4) the mapping feature of the final convolution layer is stacked on the FA and given to $L_r \in \mathbb{N}$ recurrent layer.

The convolution layer acts as a feature extractor, the recurrent layer integrates the extracted feature over time, thus giving the context data, and lastly, the feedforward layer generates the action probability for all the classes. The feedforward, convolution, and recurrent layers stack are jointly trained via backpropagation.

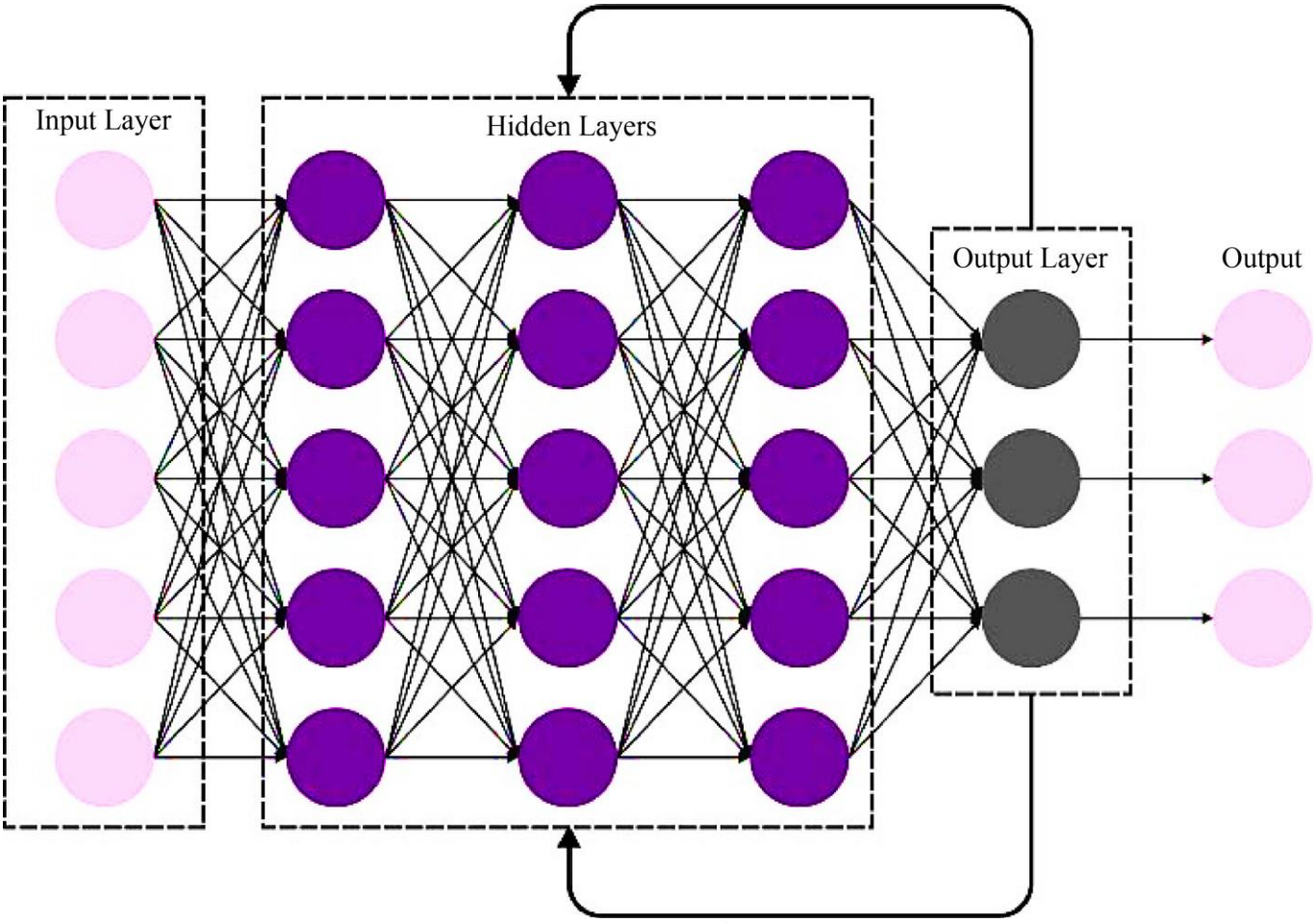

Fig. 3 Architecture of RNN

3.4.1. Convolution Layers

Context window of log mel band energy $X \in \mathbb{R}^{F\times T}$ is given as input to the CNN layer with 2D convolution sizes. After passing the feature map output through ReLU for all the CNN layers, non-overlapping max−pooling was utilized to provide more frequency invariance and decrease the data dimensionality. To maintain alignment between every target hidden activations h_t and output vector y_t. Figure 3 represents the structure of RNN.

Afterwards, in L_c convolution layers, the outcome of CNN is a tensor $\mathcal{H} \in \mathbb{R}^{M\times F'\times T}$, where F' symbolizes the number of frequency bands remaining afterwards numerous pooling functions through the CNN layer, and M represents the number of mapping features for the final CNN layer.

3.4.2. Recurrent Layers

The CNN output $H \in \mathbb{R}^{(M\cdot F')\times T}$ for $the\ L_c$ layer is given to the RNN as a series of frames $h_t^{L_c}$ afterwards stacking the feature map output over an FA. The RNN part comprises (1) The output of the final convolution layer stacked on the FA and given to the stacked recurrent layer, (2) the feedforward layer as the output layer, (3) the binarization of EA probability, and (4): L_r stacked recurrent layer every outputting and computing a h_t hidden vector for every frame as pooling in the FA.

$$\begin{aligned} h_t^{L_c+1} &= \mathcal{F}\left(h_t^{L_c}, h_{t-1}^{L_c+1}\right) \\ h_t^{L_c+2} &= \mathcal{F}\left(h_t^{L_c+1}, h_{t-1}^{L_c+2}\right) \\ &\vdots \\ h_t^{L_c+L_r} &= \mathcal{F}\left(h_t^{L_c+L_r-1}, h_{t-1}^{L_c+L_r}\right) \end{aligned} \tag{13}$$

The $\mathcal{F}$ function characterizes a GRU or LSTM unit, which has two inputs: the outcome of the prior frame of the existing layer($h_{t-1}^{L_c+1}$), and the outcome of the existing frame of the prior layer($h_t^{L_c}$).

3.4.3. Feedforward Layer

A recurrent layer followed by SLFN is utilized as the resultant layer. The feedforward layer output is derived from the final recurrent layer activation $h_t^{L_c+L_r}$ as follows

$$h_t^{L_c+L_r+1} = \mathcal{G}\left(h_t^{L_c+L_r}\right), \tag{14}$$

In Equation (14), $\mathcal{G}$ signifies a feedforward layer with sigmoid activation and employs a similar weight set for the extracted feature from all the frames.

3.4.4. Binarization

The output $h_t^{L_c+L_r+1}$ of the feedforward layer is utilized as an EA probability for all the classes $k = 1,2, \dots K$ as

$$p(y_t(k)|x_{0:t}, \theta) = h_t^{L_c+L_r+1} \tag{15}$$

Equation (15) K denotes the class count, and θ characterizes the variables of each layer of the combined network. Lastly, EA prediction $\hat{y}$ is attained by thresholding the probability over a static value $C \in [0,1]$ as follows:

$$\hat{y}_t(k) = \begin{cases} 1, & p(y_t(k)|x_{0:t}, \theta) \geq C \\ 0, & otherwise \end{cases} \tag{16}$$

4. Performance Validation

The proposed method is put under simulation on a LAPTOP-EVV5KL7B, 8GB RAM, Radeon Vega Mobile Gfx 2.10 GHz with AMD Ryzen 5 3500U, and 64-bit OS using Python 3.6.5 tool. The parameter settings are represented in the following: batch size: 5, rate of learning: 0.01, dropout: 0.5, activation: ReLU, and epoch count: 50. Figure 4 shows the sample images obtained during the preprocessing step.

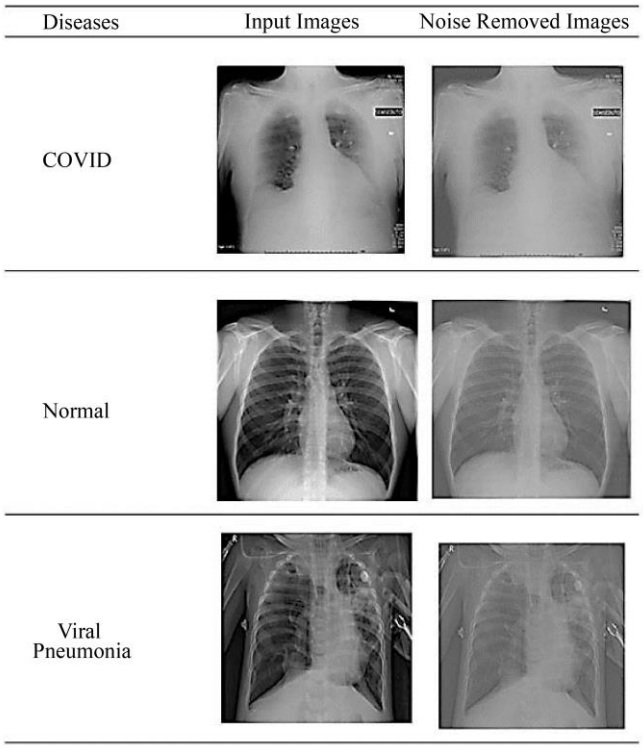

Fig. 4 Sample preprocessed images

In this study, the overall LD classification outcomes of the SLO-DCRNN technique are extensively studied on the Kaggle dataset [23]. The datasets hold 15153 samples with 3 classes, as portrayed in Table 1.

Table 1. Dataset details

Class	No. of Instances
COVID	3616
Normal	10192
Viral Pneumonia	1345
Total Number of Samples	**15153**

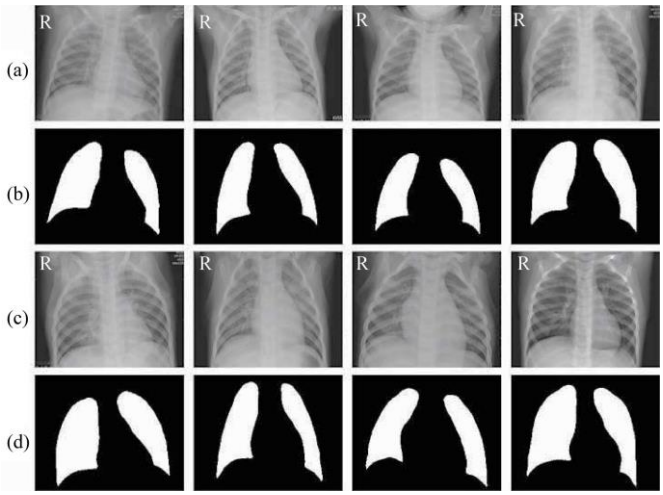

Fig. 5 Sample images (a, c) Original (b, d) Masked

Figure 5 depicts the instance imaging. Figures 5a and 5c demonstrate the original CXR images; the respective masked regions are given in Figures 5b and 5d.

Figure 6 exhibits the classifier outcomes of the SLO-DCRNN method under the testing data. Figure 6a exhibits the confusion matrix the SLO-DCRNN method offers under 70% of TRS. The figure illustrates that the SLO-DCRNN method has recognized 2514 instances of COVID, 7062 instances of normal, and 804 instances of viral pneumonia. Besides, Figure 6b describes the confusion matrix provided by the SLO-DCRNN method under 30% of TSS. The figure illustrated that the SLO-DCRNN method has analyzed 1055 instances of COVID, 3036 instances under normal, and 344 instances of viral pneumonia.

Similarly, Figure 6c illustrates the PR evaluation of the SLO-DCRNN technique. The figures show that the SLO-DCRNN technique has obtained optimum PR achievement under the overall classes. Lastly, Figure 6d denoted the ROC investigation of the SLO-DCRNN method. The figure revealed that the SLO-DCRNN method has resulted in promising outputs with the maximum values of ROC values under various class labels.

Table 2 describes the LD classification outputs of the SLO-DCRNN approach on 70% of TRS.

Table 2. LD classifier outcomes of SLO-DCRNN method on 70% of TRS

Training Phase (70%)						
Class	$Accu_y$	$Prec_n$	$Sens_y$	$Spec_y$	F_{score}	**MCC**
COVID	99.27	98.24	98.74	99.44	98.49	98.01
Normal	98.17	98.17	99.13	96.21	98.65	95.84
Viral Pneumonia	98.27	94.15	85.81	99.48	89.78	88.96
Average	**98.57**	**96.85**	**94.56**	**98.38**	**95.64**	**94.27**

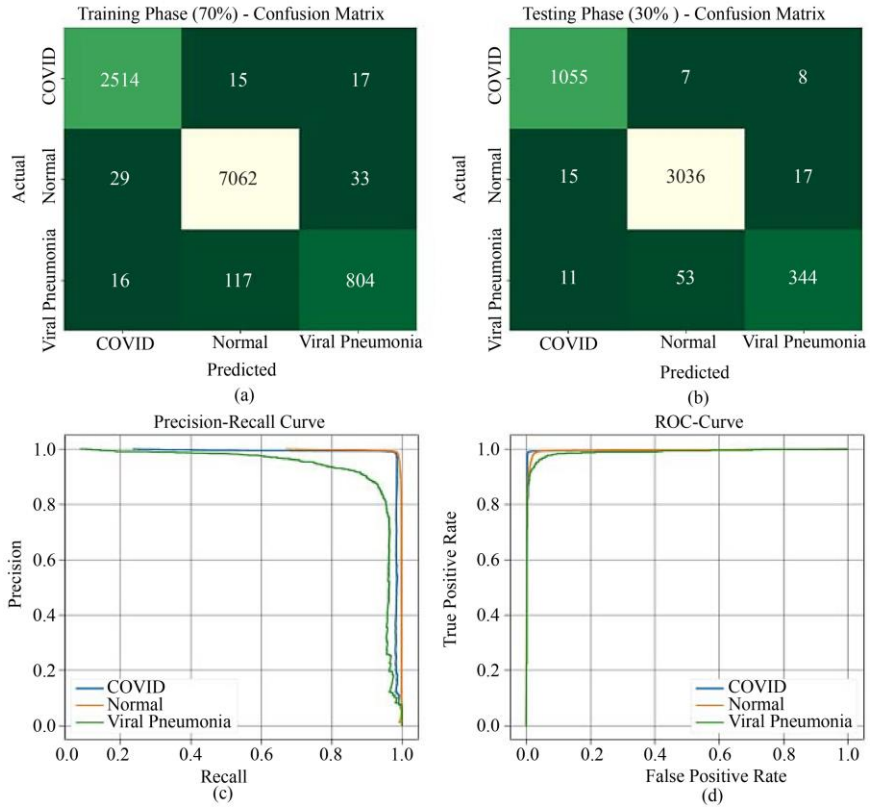

Fig. 6 Classifiers of (a-b) TRS/TSS of 70:30, (c) PR curve, and (d) ROC curve

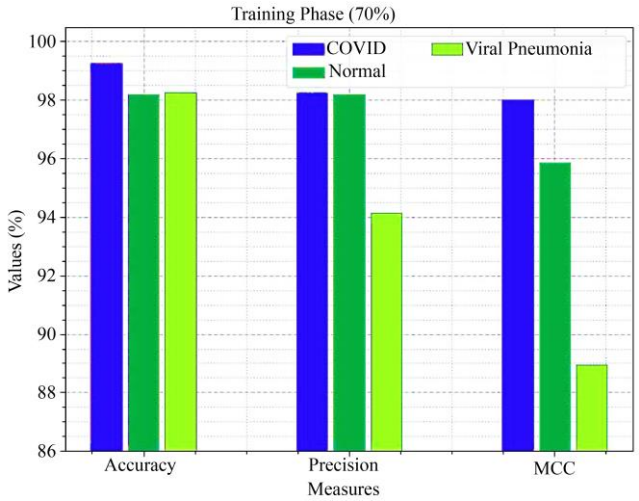

Fig. 7 $Accu_y$, $Prec_n$, and MCC outcomes of the SLO-DCRNN approach on 70% of TRS

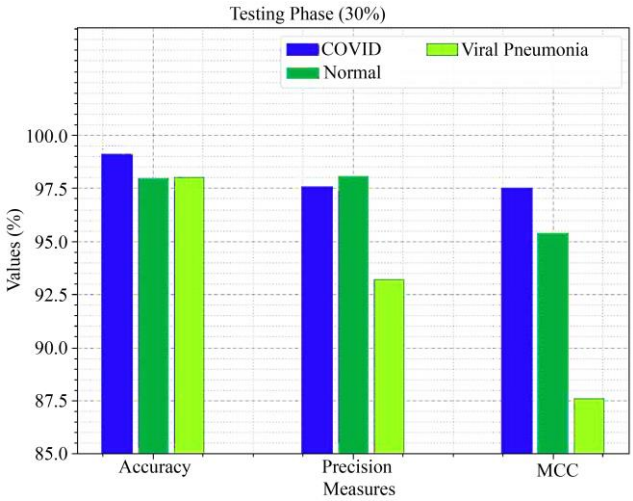

Fig. 9 $Accu_y$, $Prec_n$, and MCC outcomes of SLO-DCRNN approach on 30% of TSS

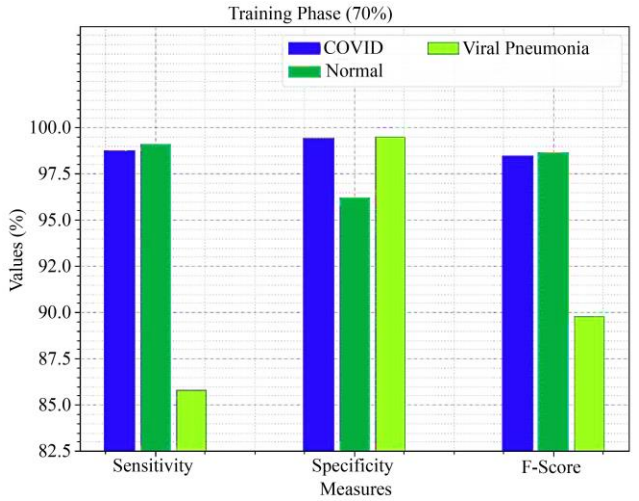

Fig. 8 $Sens_y$, $Spec_y$, and F_{score} outcomes of the SLO-DCRNN approach on 70% of TRS

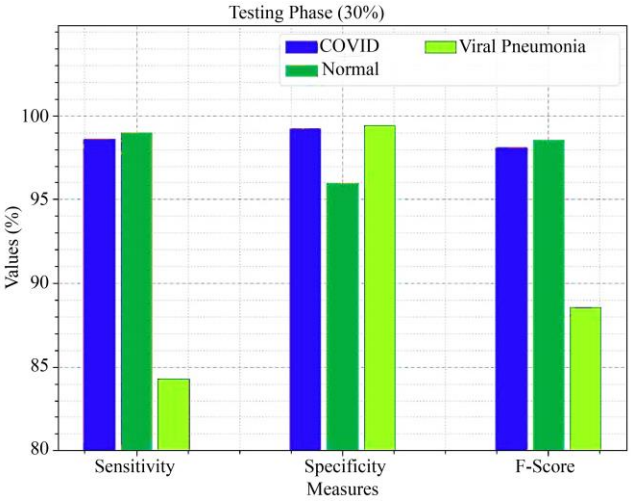

Fig. 10 $Sens_y$, $Spec_y$, and F_{score} outcomes of the SLO-DCRNN approach on 30% of TSS

In Figure 7, the overall disease detection results of the SLO-DCRNN approach are studied in terms of $accu_y$, $prec_n$, and MCC. In the COVID class, the SLO-DCRNN technique gains $accu_y$, $prec_n$, and MCC of 99.27%, 98.24%, and 98.01%, respectively. Simultaneously, in a normal class, the SLO-DCRNN technique gains $accu_y$, $prec_n$, and MCC of 98.17%, 98.17%, and 95.84% correspondingly.

Concurrently, in the viral pneumonia class, the SLO-DCRNN technique gains $accu_y$, $prec_n$, and MCC of 98.27%, 94.15%, and 88.96% correspondingly.

In Figure 8, the comprehensive disease detection results of the SLO-DCRNN technique are studied in terms of $sens_y$, $spec_y$, and F_{score}. In the COVID class, the SLO-DCRNN technique obtains $sens_y$, $spec_y$, and F_{score} of 98.74%, 99.44%, and 98.49% correspondingly.

Concurrently, in a normal class, the SLO-DCRNN method gains $sens_y$, $spec_y$, and F_{score} of 99.13%, 96.21%, and 98.65% correspondingly. Simultaneously, in the viral pneumonia class, the SLO-DCRNN method gains $sens_y$, $spec_y$, and F_{score} of 85.81%, 99.48%, and 89.78% correspondingly.

Table 3 presents the LD classification results of the SLO-DCRNN technique on 30% of TSS. In Figure 9, the overall disease detection outcomes of the SLO-DCRNN method are studied in terms of $accu_y$, $prec_n$, and MCC. In the COVID class, the SLO-DCRNN method obtains $accu_y$, $prec_n$, and MCC of 99.10%, 97.59%, and 97.51% correspondingly. Also, in a normal class, the SLO-DCRNN method achieves $accu_y$, $prec_n$, and MCC of 97.98%, 98.06%, and 95.38% correspondingly. Simultaneously, in the viral pneumonia class, the SLO-DCRNN technique gains $accu_y$, $prec_n$, and MCC of 98.04%, 93.22%, and 87.61% correspondingly.

Table 3. LD classifier outcomes of SLO-DCRNN methodology on 30% of TSS

Testing Phase (30%)						
Class	$Accu_y$	$Prec_n$	$Sens_y$	$Spec_y$	F_{score}	**MCC**
COVID	99.10	97.59	98.60	99.25	98.09	97.51
Normal	97.98	98.06	98.96	95.94	98.51	95.38
Viral Pneumonia	98.04	93.22	84.31	99.40	88.55	87.61
Average	**98.37**	**96.29**	**93.96**	**98.20**	**95.05**	**93.50**

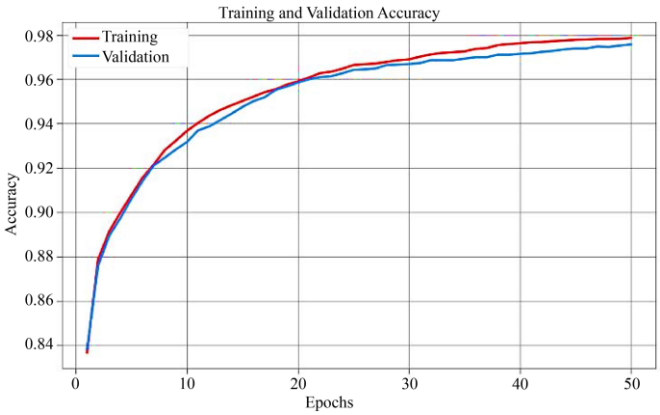

Fig. 11 TACY and VACY outcome of SLO-DCRNN method

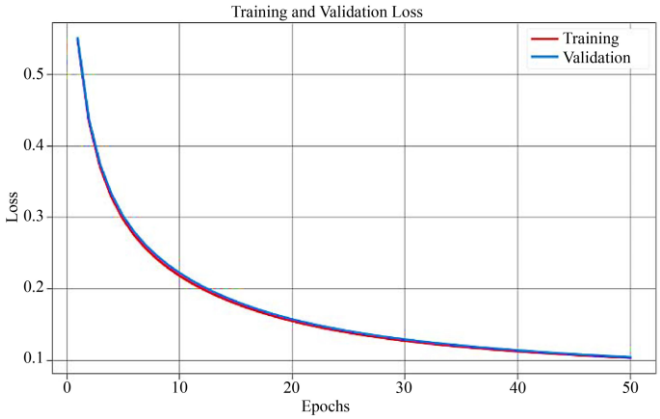

Fig. 12 TLOS and VLOS outcome of SLO-DCRNN approach

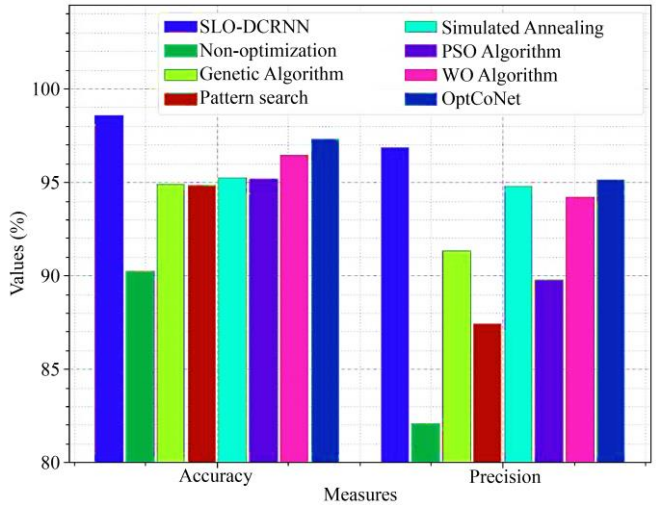

Fig. 13 $Accu_y$ and $Prec_n$ the outcome of the SLO-DCRNN approach with existing systems

In Figure 10, the overall disease detection results of the SLO-DCRNN system are studied in terms of $sens_y$, $spec_y$, and F_{score}. In the COVID class, the SLO-DCRNN method gains $sens_y$, $spec_y$, and F_{score} of 98.60%, 99.25%, and 98.09% correspondingly. In a normal class, the SLO-DCRNN method gains $sens_y$, $spec_y$, and F_{score} of 98.96%, 95.94%, and 98.51% correspondingly. Also, in the viral pneumonia class, the SLO-DCRNN technique gains $sens_y$, $spec_y$, and F_{score} of 84.31%, 99.40%, and 88.55% correspondingly.

The TACY value and VACY value of the SLO-DCRNN approach are examined on LD detection accomplishment in Figure 11. The figure showed that the SLO-DCRNN model has illustrated an enhanced accomplishment with the highest TACY values and VACY values. The SLO-DCRNN model has reached enhanced TACY outputs.

The TLOS value and VLOS value of the SLO-DCRNN approach are examined on LD recognition accomplishment in Figure 12. The figure showed that the SLO-DCRNN model has depicted the highest accomplishment with reduced TLOS and VLOS values. The SLO-DCRNN model has given a result in minimized VLOS outputs.

Finally, a comparative result of the SLO-DCRNN technique is well studied in Table 4 [24]. Figure 13 exhibits a comparison study of the SLO-DCRNN technique with existing methods in terms of $accu_y$ and $prec_n$. Based on $accu_y$, the SLO-DCRNN technique obtains increasing $accu_y$ of 98.57% while the NO, GA, PS, SA, PSO, WO, and OptCoNet techniques attain decreasing $accu_y$ of 90.22%, 94.89%, 94.82%, 95.24%, 95.16%, 96.43%, and 97.30% respectively. Besides, based on $prec_n$, the SLO-DCRNN method attains maximum $prec_n$ of 96.85% while the NO, GA, PS, SA, PSO, WO, and OptCoNet methods accomplish minimum $prec_n$ of 82.10%, 91.31%, 87.43%, 94.76%, 89.76%, 94.19%, and 95.14% correspondingly.

Figure 14 exhibits a comparison study of the SLO-DCRNN technique with existing methods in terms of $sens_y$, $spec_y$, and F_{score}. Based on $sens_y$, the SLO-DCRNN method achieves increasing $sens_y$ of 94.56%, while the NO, GA, PS, SA, PSO, WO, and OptCoNet techniques accomplish reducing $sens_y$ of 93.89%, 92.80%, 94.02%, 94.11%, 92.70%, 93.35%, and 94.20% correspondingly. Besides, based on $spec_y$, the SLO-DCRNN method attains increasing $spec_y$ of 98.38% while the NO, GA, PS, SA, PSO, WO, and OptCoNet techniques attain decreasing $spec_y$ of 89.68%, 92.43%, 93.62%, 92.62%, 95.22%, 93.98%, and 97.43% correspondingly. In addition, based on F_{score}, the SLO-DCRNN technique gains increasing F_{score} of 95.64%, while the NO, GA, PS, SA, PSO, WO, and OptCoNet systems attain decreasing F_{score} of 87.71%, 95.09%, 93.51%, 92.62%, 93.13%, 94.95%, and 94.74% correspondingly.

Table 4. Comparative outcome of SLO-DCRNN method with existing systems

Method	Accuracy	Precision	Sensitivity	Specificity	F-Score
SLO-DCRNN	**98.57**	**96.85**	**94.56**	**98.38**	**95.64**
Non-optimization	90.22	82.10	93.89	89.68	87.71
Genetic Algorithm	94.89	91.31	92.80	92.43	95.09
Pattern search	94.82	87.43	94.02	93.62	93.51
Simulated Annealing	95.24	94.76	94.11	92.62	92.62
PSO Algorithm	95.16	89.76	92.70	95.22	93.13
WO Algorithm	96.43	94.19	93.35	93.98	94.95
OptCoNet	97.30	95.14	94.20	97.43	94.74

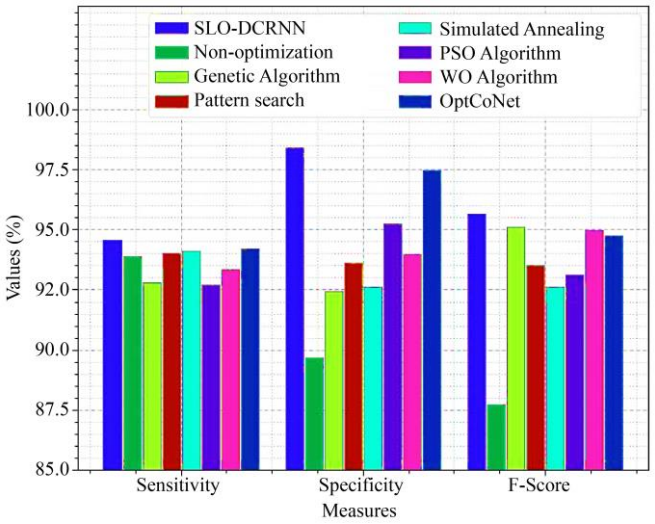

Fig. 14 $Sens_y$, $spec_y$, and F_{score} the outcome of the SLO-DCRNN approach with existing systems

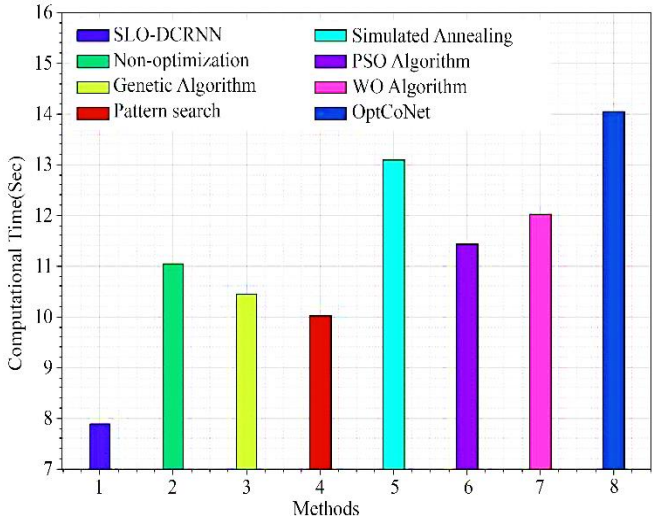

Fig. 15 Comparative CT results of the SLO-DCRNN approach

Finally, Table 5 and Figure 15 offer detailed CT results of the SLO-DCRNN technique with recent techniques. The outputs stated that the SLO-DCRNN technique accomplished better with a minimal CT of 7.89s.

At the same time, the NO, GA, PS, SA, PSO, WO, and OptCoNet techniques reached higher CT values of 11.05s, 10.45s, 10.01s, 13.10s, 11.43s, 12.03s, and 14.05s correspondingly. These results confirmed the improvements of the SLO-DCRNN method over other approaches.

Table 5. Relative CT outcome of SLO-DCRNN systems with existing models

Models	Computational Time (Sec)
SLO-DCRNN	**07.89**
Non-optimization	11.05
Genetic Algorithm	10.45
Pattern search	10.01
Simulated Annealing	13.10
PSO Algorithm	11.43
WO Algorithm	12.03
OptCoNet	14.05

5. Conclusion

This article presented a novel SLO-DCRNN approach to identify and classify lung cancer on CXR images accurately. The proposed SLO-DCRNN approach can employ the DL and hyperparameter tuning process for automated LDs. It follows a series of operations such as AWF-based noise removal, NASNet Large feature extraction, SLO-based tuning process, and DRCNN classification. The SLO-DCRNN technique primarily utilized the AWF technique to eliminate the image's noise level.

Next, the SLO-DCRNN technique employed the NASNet Large model for feature vector generation. Following this, the SLO approach was utilized for the tuning process of the DCRNN model. Finally, the DCRNN model is applied to identify different kinds of LDs.

An extensive set of investigations was accomplished to demonstrate the enhanced result of the SLO-DCRNN technique. The experimental outcome ensured the improvement of the SLO-DCRNN methodology over other existing techniques in terms of different measures.

References

[1] Vinayakumar Ravi et al., "Deep Learning-Based Meta-Classifier Approach for COVID-19 Classification using CT Scan and Images," *Multimedia Systems*, vol. 28, no. 4, pp. 1401-1415, 2022. [CrossRef] [Google Scholar] [Publisher Link]

[2] Georgios Petmezas et al., "Automated Lung Sound Classification Using a Hybrid CNN-LSTM Network and Focal Loss Function," *Sensors*, vol. 22, no. 3, pp. 1-13, 2022. [CrossRef] [Google Scholar] [Publisher Link]

[3] Shelly Soffer et al., "Artificial Intelligence for Interstitial Lung Disease Analysis on Chest Computed Tomography: A Systematic Review," *Academic Radiology*, vol. 29, pp. S226-S235, 2022. [CrossRef] [Google Scholar] [Publisher Link]

[4] Mukesh Soni et al., "Hybridizing Convolutional Neural Network for Classification of Lung Diseases," *International Journal of Swarm Intelligence Research*, vol. 13, no. 2, 2022. [CrossRef] [Google Scholar] [Publisher Link]

[5] Sungyeup Kim et al., "Deep Learning in Multi-Class Lung Diseases' Classification on Chest X-Ray Images," *Diagnostics*, vol. 12, no. 4, pp. 1-24, 2022. [CrossRef] [Google Scholar] [Publisher Link]

[6] Priya Aggarwal et al., "COVID-19 Image Classification using Deep Learning: Advances, Challenges, and Opportunities," *Computers in Biology and Medicine*, vol. 144, 2022. [CrossRef] [Google Scholar] [Publisher Link]

[7] Gopi Kasinathan, and Selvakumar Jayakumar, "Cloud-Based Lung Tumor Detection and Stage Classification Using Deep Learning Techniques," *BioMed Research International*, 2022. [CrossRef] [Google Scholar] [Publisher Link]

[8] Jiaxing Sun et al., "Detection and Staging of Chronic Obstructive Pulmonary Disease using a Computed Tomography–Based Weakly Supervised Deep Learning Approach," *European Radiology*, vol. 32, no. 8, pp. 5319-5329, 2022. [CrossRef] [Google Scholar] [Publisher Link]

[9] Eduarda M. Bortoluzzi et al., "Image Classification and Automated Machine Learning to Classify Lung Pathologies in Deceased Feedlot Cattle," *Veterinary Sciences*, vol. 10, no. 2, 2023. [CrossRef] [Google Scholar] [Publisher Link]

[10] F.M. Javed Mehedi Shamrat et al., "LungNet22: A Fine-Tuned Model for Multi-class Classification and Prediction of Lung Disease Using X-ray Images," *Journal of Personalized Medicine*, vol. 12, no. 5, pp. 1-29, 2022. [CrossRef] [Google Scholar] [Publisher Link]

[11] Thavavel Vaiyapuri et al., "Cat Swarm Optimization-Based Computer-Aided Diagnosis Model for Lung Cancer Classification in Computed Tomography Images," *Applied Sciences*, vol. 12, no. 11, pp. 1-16, 2022. [CrossRef] [Google Scholar] [Publisher Link]

[12] S. Farjana Farvin, and S. Krishna Mohan, "A Comparative Study on Lung Cancer Detection using Deep Learning Algorithms," *SSRG International Journal of Computer Science and Engineering*, vol. 9, no. 5, pp. 1-4, 2022. [CrossRef] [Publisher Link]

[13] Huiling Lu, "Computer-Aided Diagnosis Research of a Lung Tumor Based on a Deep Convolutional Neural Network and Global Features," *BioMed Research International*, 2021. [CrossRef] [Google Scholar] [Publisher Link]

[14] Feng Yang et al., "Annotations of Lung Abnormalities in the Shenzhen Chest X-ray Dataset for Computer-Aided Screening of Pulmonary Diseases," *Data*, vol. 7, no. 7, pp. 1-5, 2022. [CrossRef] [Google Scholar] [Publisher Link]

[15] K. Aravinth Raaj et al., "Automated Detection of Abnormalities in Chest X-Ray Images Using Convolutional Neural Networks," *International Journal of P2P Network Trends and Technology*, vol. 8, no. 2, pp. 18-24, 2018. [Publisher Link]

[16] C.S. Retmin Raj et al., "A Novel Feature-Significance-Based K-Nearest Neighbor Classification Approach for Computer-Aided Diagnosis of Lung Disorders," *Current Medical Imaging*, vol. 14, no. 2, pp. 289-300, 2018. [CrossRef] [Google Scholar] [Publisher Link]

[17] J. Dhalia Sweetlin, H. Khanna Nehemiah, and A. Kannan, "Computer-Aided Diagnosis of Drug-Sensitive Pulmonary Tuberculosis with Cavities, Consolidations, and Nodular Manifestations on Lung CT Images," *International Journal of Bio-Inspired Computation*, vol. 13, no. 2, pp. 71-85, 2019. [CrossRef] [Google Scholar] [Publisher Link]

[18] E. Mique Jr, and A. Malicdem, "Deep Residual U-Net-Based Lung Image Segmentation for Lung Disease Detection," *IOP Conference Series: Materials Science and Engineering*, vol. 803, no. 1, 2020. [CrossRef] [Google Scholar] [Publisher Link]

[19] Hadi Salehi et al., "A SAR Image Despeckling Method based on an Extended Adaptive Wiener Filter and Extended Guided Filter," *Remote Sensing*, vol. 12, no. 15, 2020. [CrossRef] [Google Scholar] [Publisher Link]

[20] Adedamola O. Adedoja et al., "Intelligent Mobile Plant Disease Diagnostic System Using NASNet-Mobile Deep Learning," *IAENG International Journal of Computer Science*, vol. 49, no. 1, pp. 216-231, 2022. [Google Scholar] [Publisher Link]

[21] Binh Minh Nguyen et al., "An Improved Sea Lion Optimization for Workload Elasticity Prediction with Neural Networks," *International Journal of Computational Intelligence Systems*, vol. 15, no. 1, 2022. [CrossRef] [Google Scholar] [Publisher Link]

[22] Emre Çakır et al., "Convolutional Recurrent Neural Networks for Polyphonic Sound Event Detection," *IEEE/ACM Transactions on Audio, Speech, and Language Processing*, vol. 25, no. 6, pp. 1291-1303, 2017. [CrossRef] [Google Scholar] [Publisher Link]

[23] COVID-19 Radiography Database. [Online]. Available: https://www.kaggle.com/datasets/tawsifurrahman/covid19-radiography-database/code

[24] Tripti Goel et al., "OptCoNet: an Optimized Convolutional Neural Network for an Automatic Diagnosis of COVID-19," *Applied Intelligence*, vol. 51, pp. 1351-1366, 2021. [CrossRef] [Google Scholar] [Publisher Link]